Numerical study of pressure loads generated by a shock-induced bubble collapse

Eric Goncalves da Silva, Philippe Parnaudeau

Numerical study of pressure loads generated by a shock-induced bubble collapse

Eric Goncalves da Silva[1, a)] and Philippe Parnaudeau[1]

Institut Pprime, UPR 3346 CNRS, ISAE-ENSMA, 1 avenue Clément Ader, 86961 Futuroscope Chasseneuil cedex, France.

(Dated: 11 October 2021)

This paper presents a numerical study of the strong loads caused by the collapse of an air bubble immersed in water at the vicinity of a wall and impacted by a normal shock wave. Simulations are performed using an efficient parallel fully compressible two-phase solver based on an homogeneous mixture model. Different configurations are investigated by varying the distance of the initial bubble to the wall. Comparisons are done with exiting results and with two-dimensional simulations highlighting large discrepancies on the computed pressure peaks. The computations show that the stand-off distance has significant effects on the collapse dynamics and the maximum wall pressure leading to potential wall damage. A power-law is proposed for the evolution of the maximum pressure peak as a function of the stand-off distance. Finally, a twin-bubble collapse is computed illustrating collective effects and the amplification of the pressure peak at the wall.

Keywords: Bubble collapse; Induced damage; Compressible multiphase models; Shock waves; High performance computing

[a)]Electronic mail: eric.goncalves@ensma.fr

I. INTRODUCTION

Cavitation erosion is a major problem for hydraulic and marine applications. This phenomenon occurs when vapor bubbles collapse in the vicinity of solid walls leading to negative consequences, such as vibrations, material damages and performance loss. On the other hand, cavitation can be deliberately initiated in medical applications such as shock wave lithotripsy[1] or for surface cleaning[2]. In order to find effective preventive measures, the detailed mechanism of a bubble collapse and the physical phenomena involved in the process need to be carefully investigated. To clarify the physical mechanism and to predict the bubble behaviour, numerous experimental and numerical studies of the collapse of a single bubble under shock wave loading have been proposed. The characteristic features of the bubble collapse, namely the generation and interference of intense pressure waves and the formation of high-speed jets have been minutiously investigated[3–10]. Both shock waves and high-speed jets produce high local stresses on the adjacent material surface and are responsible for material micro-deformations and damages.

Usually the numerical simulations of such a bubble collapse start from the bubble being spherical and at its maximum radius, immersed in a liquid at rest. The bubble is then collapsed by the impact of a normal incident shock wave or due to a driving pressure difference. During the collapse, different pressure peaks on the wall are registered corresponding to the impact of the high-speed liquid jet and the shock waves emitted upon the collapse[11,12]. It is known that the dynamics is strongly influenced by the stand-off parameter Γ, which is defined by the ratio of the distance between the initial bubble center and the wall L and the initial bubble radius R_0. The influence of this parameter has been investigated by various authors and the potential damage to the neighbouring surfaces has been quantified by measuring the wall pressure. In the experimental study of Shima et al. using a spark discharge to generate a cavitation bubble[13], three types of the bubble collapse modes were highlighted: i) a type where the shock wave is dominant to the impact wall pressure, at $\Gamma < 0.3$ and > 1.5, ii) a type where the liquid jet is dominant, at $0.6 < \Gamma < 0.8$, and iii) a type where both a shock wave and a liquid jet coexist, at $0.3 < \Gamma < 0.6$ and $0.8 < \Gamma < 1.5$. For $0.8 < \Gamma < 1.2$, a splashing behaviour was observed[14,15] representing the migration of the bubble torus into water in a direction perpendicular to the wall and forming a mushroom shaped cavity. For cavitation bubbles growing very close to the wall ($\Gamma < 1$) the impact of the high-speed liquid jet onto the material surface and the shear forces acting along the wall surface play a major role[16].

In their numerical study using fluid-structure coupled simulations, Choi and Chahine[17] concluded that the stand-off distance affected the high-speed jet characteristics in a non-monotonic fashion. However, a higher jet velocity did not necessarily result in a higher impact pressure. Moreover, the shape of the pit did not vary monotonically with the stand-off distance. Another work by Turangan et al.[18] simulated the bubble collapse near a rigid Aluminium wall with different stand-off distance and found that an attached cavity can produce larger deformation compared to a detached cavity. Such results were corroborated by Joshi et al. using Smoothed Particle Hydrodynamics (SPH) simulations[19]. On another hand, multiple shock waves may be emitted during the collapse: one due to the impact of the high-speed jet on the opposite interface of the bubble (water-hammer shock), shocks due to the collapse of a small volume trapped between the jet tip and the opposite interface of the bubble (tip bubble shock waves) and other waves due to the recollapse of the toroidal ring[10,20,21]. The order in which the shocks are generated depends on the stand-off distance.

The computation of bubble collapses and the induced damage is challenging. To simulate this kind of stiff compressible two-phase flows, various approaches have been proposed which can be categorized into two main classes, namely interface-tracking methods (sharp interface) and interface-capturing methods (diffuse interface). With interface-tracking methods, the location of the interfaces, treated as sharp discontinuities, is explicitly represented during the time evolution[22–26]. On the other hand, diffuse interface methods are based on the solution of conservation laws (continuity, momentum, and energy equations), while relaxing the sharp character of material interfaces and thus allowing them to numerically diffuse over a small but finite region[27–31]. An alternative to the above-mentioned numerical methods is the use of the Boundary Element Method (BEM), where only the surface of the bubble is meshed[16,32,33]. However, in BEM, the model is based on potential incompressible flow. Besides, due to the fast dynamics and the extreme violence of the collapse - the pressure amplitudes can reach a few GigaPascal and the jet velocity can reach over 1000 m/s - the simulation of such problems induces the need of refined computational grids and very small time steps. Computational grids can reach over 1 billion nodes leading to a large Central Processing Unit (CPU) cost. As a consequence, simulations require not only an accurate model to capture the large variation of material properties and the complex shock-interface interactions correctly, but also an efficient parallel strategy to manage the necessary large resolution near interfaces. Yet, most of computations in the literature have been limited to two dimensions or axisymmetric descriptions. Up to now, only few detailed three-dimensional

simulations have been proposed[34–38].

Despite numerous studies, the influence of the stand-off parameter on the bubble dynamics and more specifically the understanding of the contribution of the different generated shock waves to the material damage as well as the role of the jet is still not fully understood[10,39]. In regard to the prediction of cavitation erosion rates, a key point is the response of the material to impact loads in bubble collapses. An estimation of the peak pressure at the wall is thus of primary interest. In the present work, three-dimensional simulations are performed on a shock-induced bubble collapse near a rigid wall. The influence of the stand-off distance is investigated for a wall-detached bubble with a special care to the relevant waves emission and wall impact. We use an in-house compressible multiphase solver based on a homogeneous mixture approach and a massive parallel strategy[37,40]. A particular attention is paid on the maximum values of the wall pressure reached during the process. Comparisons are done with existing results and with 2D simulations performed with the same solver. Viscous effects are evaluated on different 2D simulations. In the study of Hawker and Ventikos[8] where spherical and cylindrical bubble collapses were compared, authors reported 40% higher pressure for a spherical bubble compared to a cylindrical one. In the present study, we show that the maximum pressure peak monitored at the wall can be largely higher for the spherical collapse, suggesting high stresses that can exceed the local material yield stress. Moreover, a power-law is proposed for the maximum wall pressure as a function of the stand-off parameter. Different authors tried to link the characteristic erosion pattern to the local flow field by the use of 3D simulations[41]. Such a law will serve the development of low-order models for bubble collapse and will feed empirical erosion criteria or indicators. Finally the study of collective effects and the potential amplification of the pressure peaks on the wall is proposed. The dynamics of such configurations, for which simulations in three dimensions are very scarce in the literature (see for example the recent work of Bempedelis and Ventikos[36] for different bubble arrays collapsing without the presence of a wall), are significantly different from those in two dimensions. Here, a simple configuration is considered, namely two bubbles of the same size impacted by a normal shock wave. The highest pressures and the relevant processes are analysed.

The paper is organized as follows. In section II, we first review the theoretical formulation, models and numerical methods. Then, preliminary results are proposed in section III for a free-field case and to attest the mesh convergence. Viscous effects are also discussed. In section IV

the cylindrical collapse near a wall is investigated when the stand-off distance is varying. Then, 3D results are presented in section V followed by a discussion on the influence of the stand-off parameter. Collective effects are illustrated in Section VI. Finally, conclusions and future investigations are given.

II. EQUATIONS AND MODELS

The numerical simulations are carried out using an in-house, two-phase code solving a one-fluid compressible system. It is assumed that phases evolute at the same velocity. In addition, the phases are assumed to be in mechanical and thermal equilibrium, leading to a one-pressure and one-temperature model.

Weber numbers $W_e = \rho U^2 D/\sigma$ based on bubble diameter and jet velocity (around 800 m/s) are higher than 8×10^6. Thus, surface tension effects are dominated by inertia and are neglected. Phase change is not expected to affect the bubble dynamics over the major part of the collapse and is therefore ignored. The question of viscous effects has been discussed by different authors[7,26,42]. To assess the influence of these effects, inviscid and viscous simulations will be compared (see Section III).

A. Governing equations

The model consists in three conservation laws for mixture quantities (mass, momentum and total energy) and the additional equation for the void ratio α (see[43] for more details). The inviscid system is expressed as:

$$\frac{\partial \rho}{\partial t} + \mathrm{div}(\rho \mathbf{V}) = 0 \tag{1}$$

$$\frac{\partial (\rho \mathbf{V})}{\partial t} + \mathrm{div}(\rho \mathbf{V} \otimes \mathbf{V} + P I_\mathrm{d}) = 0 \tag{2}$$

$$\frac{\partial (\rho E)}{\partial t} + \mathrm{div}(\rho \mathbf{V} H) = 0 \tag{3}$$

$$\frac{\partial \alpha}{\partial t} + \mathbf{V}.\mathrm{grad}(\alpha) = \underbrace{\left(\frac{\rho_l c_l^2 - \rho_g c_g^2}{\frac{\rho_l c_l^2}{1-\alpha} + \frac{\rho_g c_g^2}{\alpha}} \right)}_{=K} \mathrm{div}(\mathbf{V}) \tag{4}$$

where P is the pressure, ρ the mixture density, $\mathbf{V}$ the center of mass velocity vector, $E = e + V^2/2$ denotes the total energy, e the internal energy, $H = h + V^2/2$ the total enthalpy and h the enthalpy.

I_d is the identity matrix. Subscripts l and g for liquid and gas, respectively. The term K involves the speed of sound of pure phases c_k and it reflects the effects of changes in volume of each phase. It describes the reduction (or the increase) of the volume fraction of gas in a mixture when a compression wave (or an expansion wave) travels across the mixing region. The importance of this term has been reported in the works of Tiwari et al.[44] and Wermelinger et al.[35] using a five-equation model. A comparison of the four and five-equation models has been recently proposed for the simulation of shock-induced bubble collapse[37]. This study clearly showed the capability of the four-equation model to reproduce as correctly as the five-equation model the physical phenomena with a much lower computational cost.

We used the convex stiffened gas equation of state (EOS) for both the pure phases. From the thermal and mechanical equilibrium assumption, an expression for the mixture pressure and temperature can be deduced :

$$P(\rho,e,\alpha,Y) = (\gamma(\alpha)-1)\rho(e-q(Y)) - \gamma(\alpha)P_\infty(\alpha) \tag{5}$$

$$T(\rho,h,Y) = \frac{h-q(Y)}{C_p(Y)} \quad \text{with} \quad C_p(Y) = YC_{p_g} + (1-Y)C_{p_l} \tag{6}$$

$$\frac{1}{\gamma(\alpha)-1} = \frac{\alpha}{\gamma_g-1} + \frac{1-\alpha}{\gamma_l-1} \quad \text{and} \quad q(Y) = Yq_g + (1-Y)q_l \tag{7}$$

$$P_\infty(\alpha) = \frac{\gamma(\alpha)-1}{\gamma(\alpha)}\left[\alpha\frac{\gamma_g}{\gamma_g-1}P_\infty^g + (1-\alpha)\frac{\gamma_l}{\gamma_l-1}P_\infty^l\right] \tag{8}$$

where $Y = \alpha\rho_g/\rho$ is the mass fraction of gas, $\gamma = C_p/C_v$ is the heat capacity ratio, C_p and C_v are thermal capacities, q the energy of formation of the fluid and P_∞ is a constant reference pressure. The system of equations is hyperbolic and the speed of sound follows the Wallis or Wood formulation[45]:

$$\frac{1}{\rho c_{wallis}^2} = \frac{\alpha}{\rho_g c_g^2} + \frac{1-\alpha}{\rho_l c_l^2} \tag{9}$$

To evaluate the influence of viscous effects on the bubble collapse, the viscous terms are included in the one-fluid system. We introduce the mixture stress sensor $\overline{\overline{\tau}}$ evaluated using the Stokes' hypothesis and the Newton's law for each phase and the mixture heat flux vector $\mathbf{Q}$ obtained from the Fourier law for each phase:

$$\begin{aligned}\overline{\overline{\tau}} &= \mu\left[\operatorname{grad}\mathbf{V} + (\operatorname{grad}\mathbf{V})^{\mathbf{t}} - \frac{\mathbf{2}}{\mathbf{3}}(\operatorname{div}\mathbf{V})\mathbf{I_d}\right]\\ \mathbf{Q} &= -\lambda\operatorname{grad}T\end{aligned} \tag{10}$$

where $\mu(\alpha,T)$ and $\lambda(\alpha,T)$ are the mixture viscosity and the mixture thermal conductivity, respectively. These quantities are defined as the arithmetic mean of the liquid and gas phasic values (fluctuations are neglected)[46].

In the pure liquid, the viscosity is determined by an exponential law and, in pure gas, the viscosity follows Sutherland's law:

$$\mu_l(T) = \mu_{0_l} \exp(B/T) \tag{11}$$

$$\mu_g(T) = \mu_{0_g} \sqrt{\frac{T}{293}} \frac{1+T_S/293}{1+T_S/T} \tag{12}$$

$$\mu(T,\alpha) = \alpha\mu_g(T) + (1-\alpha)\mu_l(T) \tag{13}$$

where μ_{0_l}, μ_{0_g}, B and T_S are constant parameters.

The mixture thermal conductivity is expressed through the phasic Prandtl numbers:

$$\lambda(\alpha,T) = \alpha\frac{\mu_g(T)C_{p_g}}{P_{r_g}} + (1-\alpha)\frac{\mu_l(T)C_{p_l}}{P_{r_l}} \tag{14}$$

with $P_{r_g} = 0.72$ and $P_{r_l} = 7$.

B. Numerical methods

The fluid solver is based on a cell-centered finite-volume discretisation on Cartesian grids with an explicit temporal integration. The PDE inviscid system can be represented in a matrix form as:

$$\frac{\partial U}{\partial t} + \mathrm{div}\,[F(U)] + B(U)\,\mathrm{div}\mathbf{V} = 0 \tag{15}$$

with $U = (\rho, \rho\mathbf{V}, E, \alpha)$ denotes the conservative variables and the void ratio, $F(U) = (\rho\mathbf{V}, \rho\mathbf{V}\otimes\mathbf{V} + PI_d, \alpha\mathbf{V})$ the flux vector and $B(U) = (0, \mathbf{0}, 0, -(K+\alpha))$ the source term. By considering a cell ($\mathscr{C}_i$) with a volume (Ω_i) delimited by a surface ($\partial\mathscr{C}_i$) of outward normal $\mathbf{n_i}_{,\ell}$ of cell interface ℓ, the integration of the system gives:

$$\Omega_i\frac{\partial U_i}{\partial t} + \sum_{\ell\in\partial\mathscr{C}_i}\int_\ell F(U)\cdot\vec{n}_{i,\ell}\,d\ell + \tilde{B}_i\sum_{\ell\in\partial\mathscr{C}_i}\int_\ell \mathbf{V}\cdot\vec{n}_{i,\ell}\,d\ell = 0 \tag{16}$$

where $\tilde{B}_i$ is some average of B on cell $\mathscr{C}_i$.

The numerical flux $\tilde{F}_{i,\ell}$ through the cell interface ℓ is computed with a HLLC scheme[37,47]. The temporal integration is performed with a fix time-step Δt that respects the Courant-Friedrichs-Lewy condition. In order to obtain the second-order in both space and time, the TVD MUSCL-Hancock method[48] is implemented by considering the three following steps.

1. Reconstruction of the solution via piecewise linear functions. In regard to robustness considerations, primitive variables $W = (\rho, \mathbf{V}, P, \alpha)$ are chosen and the minmod slope limiter is used.

2. Advance of the solution by half time-step $\Delta t/2$ before the derivation of time-centered interface values. With the use of primitive variables, the system of equations is rewritten in the quasi-linear form by introducing a matrix $A_{w,\ell}$. It reads:

$$W_i^{n+1} = W_i^n - \frac{\Delta t}{2} \sum_{\ell \in \partial \mathscr{C}_i} \frac{1}{\Delta x_l} A_{w,\ell} \Delta W_{i\ell} \tag{17}$$

The expression of matrices can be easily computed and is given only for the x-direction:

$$A_{w,x} = \begin{bmatrix} \mathbf{V}\cdot\mathbf{n_x} & \rho & 0 & 0 & 0 & 0 \\ 0 & \mathbf{V}\cdot\mathbf{n_x} & 0 & 0 & 1/\rho & 0 \\ 0 & 0 & \mathbf{V}\cdot\mathbf{n_x} & 0 & 0 & 0 \\ 0 & 0 & 0 & \mathbf{V}\cdot\mathbf{n_x} & 0 & 0 \\ 0 & \rho c_{wallis}^2 & 0 & 0 & \mathbf{V}\cdot\mathbf{n_x} & 0 \\ 0 & -K & 0 & 0 & 0 & \mathbf{V}\cdot\mathbf{n_x} \end{bmatrix}$$

3. Solve the Riemann problem with the HLLC scheme to update the conservative variables.

The numerical treatment of the boundary conditions is based on the use of the characteristic relations of the four-equation system[37]. The dissipative fluxes are discretized by a second-order space-centered scheme. The software is designed for high performance computing (HPC) and is parallelized with a hybrid paradigm using the MPI, OpenMP and openACC programming models (see[49] for more details).

III. VALIDATION AND PRELIMINARY RESULTS

The code has been validated on various 1D and 2D compressible two-phase flows[40,50] and on the case of a spherical helium bubble immersed in air and impacted by a normal shock wave[37]. To assess the ability of the numerical tool to compute efficiently a bubble collapse located in a liquid medium, we present the benchmark of the bubble collapse in a free-field by comparison with analytical solution. Then, preliminary 2D and 3D results dealing with the study of the mesh

influence are presented on a stiff shock-induced bubble collapse. Finally, the influence of viscous effects on the pressure loads is studied.

A. Bubble collapse in a free-field

The study consists of simulating the collapse of a gas bubble with an initial internal pressure P_g and an initial radius $R_0 = 1$ mm immersed in water at rest at the pressure P_l. The collapse is driven by the pressure jump $\frac{P_l}{P_g} = 353$. Parameters of the EOSs are:

$$\begin{pmatrix} \gamma \\ P_\infty \\ C_p \end{pmatrix}_{\text{Liquid}} = \begin{pmatrix} 2.35 \\ 10^9 \text{ Pa} \\ 4267 \text{ J/kg.K} \end{pmatrix} \quad ; \quad \begin{pmatrix} \gamma \\ P_\infty \\ C_p \end{pmatrix}_{\text{Gas}} = \begin{pmatrix} 1.43 \\ 0 \text{ Pa} \\ 1487 \text{ J/kg.K} \end{pmatrix}$$

This configuration allows to compare the evolution of the effective bubble radius R with the solution resulting from the Keller-Miksis equation[51]. The effective bubble radius is defined as:

$$\mathrm{R} = \left(\frac{3V_g}{4\pi}\right)^{1/3} \quad \text{with} \quad V_g = \int \alpha \mathrm{d}\Omega$$

where V_g is the total volume of gas.

Using the symmetry of the problem, only a quarter of the bubble is considered. The computational domain, relative to the initial bubble radius R_0, is $[L_x \times L_y \times L_z] = [100R_0 \times 50R_0 \times 50R_0]$. It is taken large enough to minimize the impact of the boundary conditions. The position of the bubble center is $(50R_0, 0, 0)$. Non-reflecting conditions are applied on the faces of the domain. The number of points per initial bubble radius N_r varies from 10 to 30 to evaluate the grid refinement influence. A dimensionless time $t^* = t/t_R$ is introduced for the validation where t_R is the Rayleigh time. This collapse time can be estimated by the relation[52]:

$$t_R = 0.915 R_0 \sqrt{\frac{\rho_l}{P_l - P_g}}$$

The time evolution of the dimensionless bubble radius R/R_0 is illustrated in Figure 1 for all meshes. Simulations are performed with and without the term $K\mathrm{div}\mathbf{V}$ appearing in the void ratio equation in order to evaluate the influence of this quantity. A very good agreement between the numerical result obtained with the finest grid and the Keller-Miksis solution is observed. Moreover, the effect of the source term is clearly highlighted: the quantity $K\mathrm{div}\mathbf{V}$ in the four-equation model provides a significantly more accurate result, especially at the minimum radius around time

$t^* = 1.1$ (the difference between models reaches a factor of 3). Such a behaviour underlines the importance to consider this contribution in the void ratio transport equation for properly capturing the dynamics of collapsing bubbles.

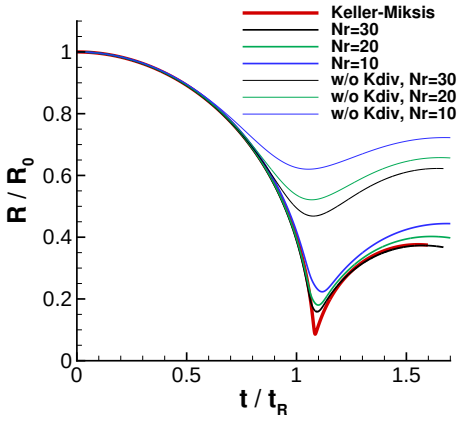

FIG. 1. Time evolution of the effective bubble radius R/R_0 for the collapse with $P_l/P_g = 353$.

B. Shock-induced bubble collapse: mesh influence

The considered test is similar to the one presented in the study of Paquette et al.[53]. An air bubble, 0.05 mm in initial radius, is immersed in a water pool at rest, under the following initial conditions: $P = 10^5$ Pa, $T = 298$ K, ρ_{air} = 1.176 kg/m^3 and ρ_{water} = 1000 kg/m^3. The bubble is collapsed by a normal shock wave moving at $M_{sh} = 1.042$, corresponding to an amplitude of 120 MPa, and initially located at a distance R_0 from the bubble as shown in Figure 2.

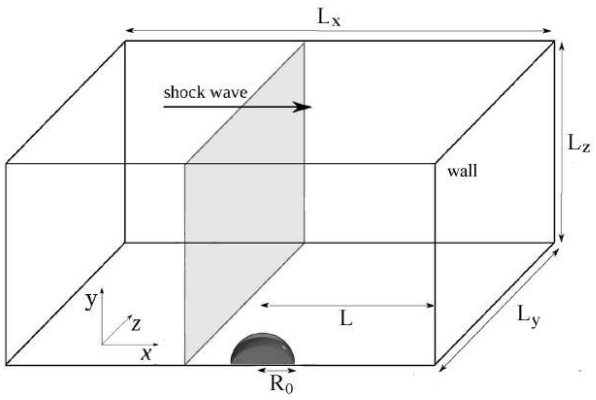

FIG. 2. Configuration at initial time, M_{sh}=1.042.

Parameters of the EOSs and post-shock conditions are:

$$\begin{pmatrix} \gamma \\ P_\infty \\ C_p \end{pmatrix}_{\text{liquid}} = \begin{pmatrix} 2.35 \\ 10^9 \text{ Pa} \\ 5844 \text{ J/kg.K} \end{pmatrix} ; \begin{pmatrix} \gamma \\ P_\infty \\ C_p \end{pmatrix}_{\text{gas}} = \begin{pmatrix} 1.4 \\ 0 \text{ Pa} \\ 1009 \text{ J/kg.K} \end{pmatrix} ; \begin{pmatrix} \text{P} \\ \rho \\ \text{u} \end{pmatrix}_{\text{post-sh}} = \begin{pmatrix} 1.2 \times 10^8 \text{ Pa} \\ 1049.32 \text{ kg/m}^3 \\ 75.07 \text{ m/s} \end{pmatrix}$$

The ratio $\Gamma = L/R_0$ between the position of the bubble center to the wall and the initial bubble radius is a major parameter that governs the bubble collapse dynamics. As suggested in the study of Johnsen and Colonius[7], the bubble initially located at a distance lower than L/R_0= 2 presents a high potential to cause damage. We consider in this section only the case where the ratio $L/R_0 = 2$.

A study of the mesh influence is conducted to ensure that grid independence is achieved for the 2D cylindrical configuration. Due to the symmetry of the problem, we only consider a half bubble. The computational domain size, relatively to the initial bubble radius R_0, is $[L_x \times L_y] = [6R_0 \times 10R_0]$. The boundary conditions are the following: the top and bottom boundaries are assumed to be a wall and a symmetry axis, respectively. The left and right sides are assumed to be non-reflecting and a wall, respectively. Five meshes with an increased refinement are computed, from 600×1000 cells to 1500×2500 cells, which correspond to a number of points per initial bubble radius $N_r = [100, 125, 150, 200, 250]$, respectively. Computations are performed with a constant CFL value equal to 0.3. To evaluate the grid convergence, the dimensionless maximum

wall pressure reached during the collapse is plotted in Figure 3, on the left part, for all considered meshes. This quantity is obtained by dividing it by the incident shock pressure P_{sh}.

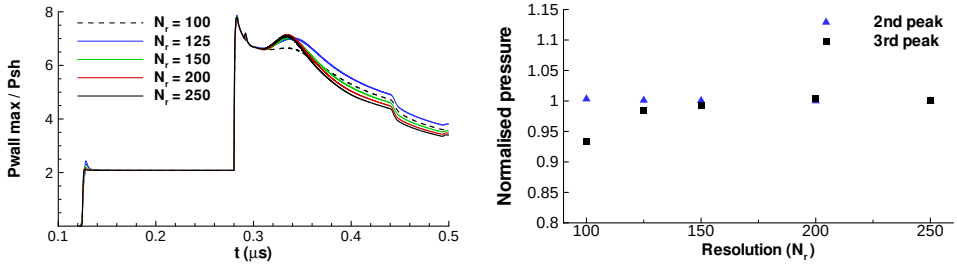

FIG. 3. Effect of the grid resolution for the 2D cylindrical collapse with $L/R_0 = 2$: evolution of the dimensionless maximum wall pressure reached during the collapse (left) and pressure peaks during the collapse normalized by the value obtained with the finest grid (right).

We can observe different pressure peaks due to wave impacts (the description of phenomena will be done in the next paragraph). Considering the most intense peak, both the time of impact and the intensity do not vary with the mesh. This pressure peak converges rapidly with the grid resolution. At a later time, around time $t = 0.34$ μs, discrepancies between solutions are noticeable. The intensity of the main pressure peaks are plotted in the right part of the figure, normalized by the value obtained using the finest grid. The plotted values correspond to the peak monitored at time $t = 0.28$ μs (referenced as 2nd peak) and the peak monitored at time $t = 0.34$ μs (referenced as 3rd peak). The second pressure peak converges rapidly with the grid resolution. More variation is illustrated for the third pressure peak. Based on these results, the grid composed by 900×1500 cells corresponding to $N_r = 150$ is viewed sufficient to capture the wall pressure evolution.

Due to the prohibitive computational cost, a complete study of the mesh influence for the 3D spherical case is not practical. Only two meshes are considered for which the number of nodes per initial bubble radius N_r is 55 and 110, respectively. Exploiting the symmetry of the problem preserved on the major part of the collapse, only a quarter of the bubble is computed. The computational domain is $[L_x \times L_y \times L_z] = [8R_0 \times 12R_0 \times 12R_0]$ and the initial position of the bubble is $(6R_0, 0, 0)$. Computations are performed with a constant CFL value equal to 0.15 and the finest grid reaches 1.5 billion of nodes. All simulations are run on the supercomputer resource of IDRIS

using more than 2000 processors. Similar to the 2D configuration, the grid convergence is evaluated on the dimensionless maximum pressure reached during the collapse, either in the fluid or along the wall, as plotted in Figure 4. The mesh effect on the most intense peak in the fluid around time $t = 1.7\,10^{-7}$ s is clearly illustrated (the gap is close to 20%). Yet, in regard to the most intense pressure peak on the wall around time $t = 1.9\,10^{-7}$ s, the mesh influence is very weak. Based on these results, the grid corresponding to $N_r = 110$ is selected in the following of the study.

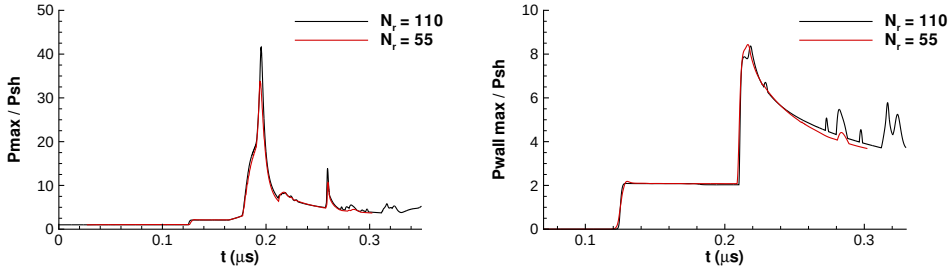

FIG. 4. Effect of the grid resolution for the 3D spherical collapse with $L/R_0 = 2$: evolution of the dimensionless maximum pressures in the fluid (left) and along the wall (right).

C. Shock-induced bubble collapse: viscous effects

We consider the same test case by taking into account viscous effects in the formulation. Simulations are performed on the same regular grid 900×1500 nodes and with 3 values of the stand-off distance: $L/R_0 = 2$, 1.4 and 1.1. The x_+ values in the first adjacent cells to wall vary between 0.1 and 12. A reduction of the time step by a factor 2 was necessary to obtain results for cases $L/R_0 = 1.4$ and 1.1, leading to an increase of the computational cost.

The dimensionless maximum pressures inside the fluid and along the wall are plotted in Figure 5 compared to the inviscid computations. Results are superposed during a large part of the process for all stand-off parameters. For $L/R_0 = 2$ and 1.4, the intensity of the strongest pressure peak is identical. Discrepancies appear after the impact of the water-hammer shock on the wall, the viscous solution being a little smaller than the inviscid one. For the stand-off distance $L/R_0 = 1.1$, the maximum pressure peak in the fluid (corresponding to the recollapse of bubble pieces) obtained with the viscous simulation is slightly higher. At the wall, the pressure peaks

provided by both simulations are identical. In regard to these results, the computation of pressure loads is not influenced by viscous effects and all simulations presented in the following will not consider these terms.

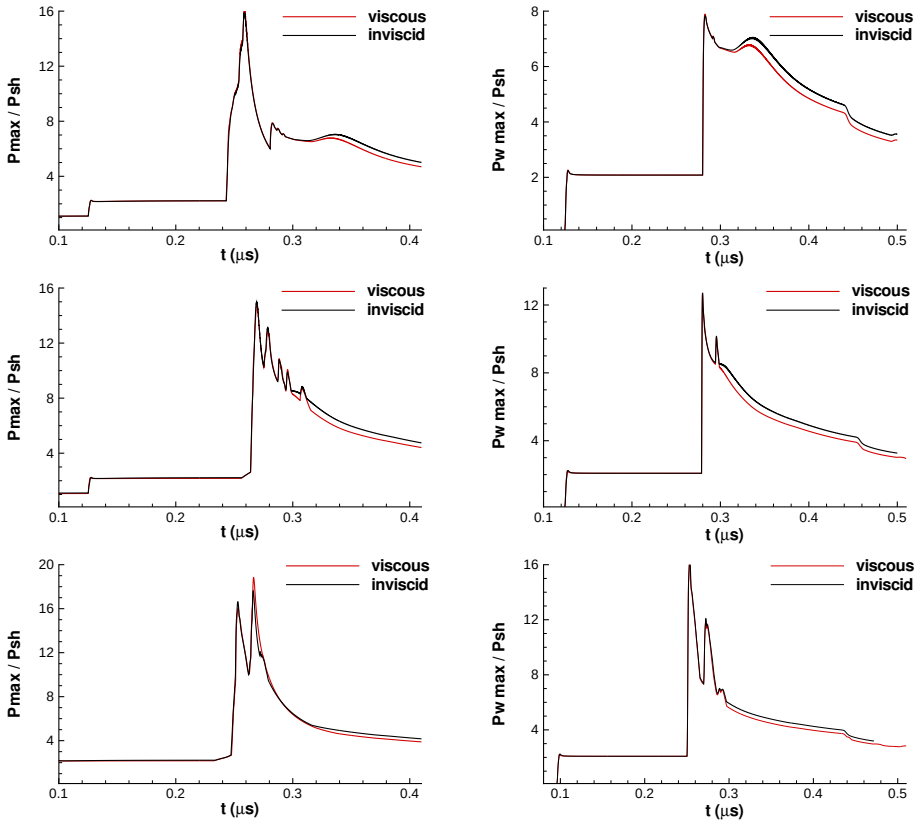

FIG. 5. Viscous effects for the 2D cylindrical collapse with a stand-off parameter $L/R_0 = 2$ (top), $L/R_0 = 1.4$ (middle) and $L/R_0 = 1.1$ (down). Evolution of the dimensionless maximum pressures in the fluid (left) and along the wall (right).

IV. INVESTIGATION OF THE CYLINDRICAL BUBBLE COLLAPSE

We performed different simulations by varying the stand-off distance L/R_0 from 2 to 1.05. All simulations were done using a constant time step $\Delta t = 10^{-10}$ s and the same grid with $N_r = 150$

as discussed in the last section.

A. Case $L/R_0 = 2$

A qualitative description of the main phenomena involved in this interaction is firstly proposed. The time evolution of the density gradient modulus (Schlieren-type representation) are plotted in Figure 6 from time $t = 0.08$ μs to $t = 0.36$ μs. After the incident shock wave has collided with the bubble, a rarefaction wave is reflected backwards from the interface and a weak shock wave is transmitted inside of the bubble (time $t = 0.08$ μs). The incident shock impacts the wall and reflects (time $t = 0.14$ μs), which generates the first pressure peak on the wall (see Figure 3). The reflected shock wave propagates backwards and collides with the bubble (time $t = 0.18$ μs). The pressure difference between both sides of the bubble induces a high-speed jet of water along the axis of flow symmetry (time $t = 0.22$ μs). When this water jet impacts the right interface of the bubble (time $t = 0.24$ μs), an intense blast wave (also called water-hammer shock) is formed generating a high-pressure area in the fluid. The blast wave propagates asymmetrically on both directions (time $t = 0.26$ μs) and the rightward wave increases as a circular wave. At time $t = 0.28$ μs, the rightward front wave impacts the wall and reflects, generating the most intense pressure peak on the wall (see Figure 3). At time $t = 0.32$ μs, we can observe the propagation of the blast wave and the reflected blast wave which collides with the bubble pieces, generating other waves. Multiple wave reflections between the wall and the bubble are illustrated at time $t = 0.36$ μs, suggesting extensive regions of high pressure.

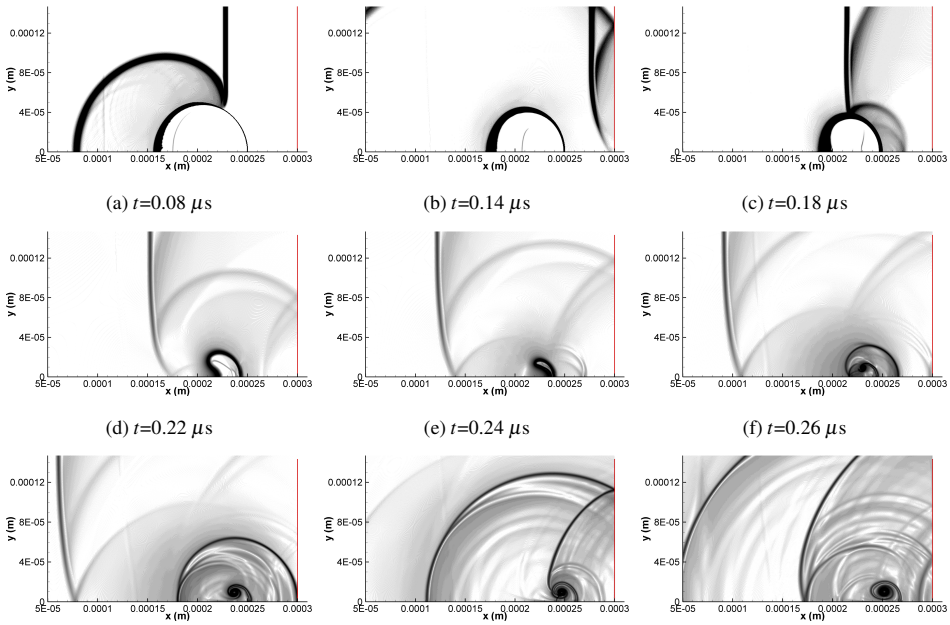

(a) t=0.08 μs (b) t=0.14 μs (c) t=0.18 μs

(d) t=0.22 μs (e) t=0.24 μs (f) t=0.26 μs

(g) t=0.28 μs (h) t=0.32 μs (i) t=0.36 μs

FIG. 6. Evolution of the density gradient for the 2D case $L/R_0 = 2$ at different times: a) t=0.08 μs, b) t=0.14 μs, c) t=0.18 μs, d) t=0.22 μs, e) t=0.24 μs, f) t=0.26 μs, g) t=0.28 μs, h) t=0.32 μs and i) t=0.36 μs.

B. Case $L/R_0 = 1.1$

We consider now the case where the bubble is very close to the wall with the ratio $L/R_0 = 1.1$. A qualitative description is proposed based on the time evolution of the density gradient modulus plotted in Figure 7. The beginning of the interaction is similar to the previous case. At time $t = 0.14$ μs, the incident shock has reflected on the wall and collides with the bubble. The reflected shock wave passes the bubble, which is asymmetrically contracted (times $t = 0.2$ μs and $t = 0.26$ μs) with the penetration of the water jet. This high-speed jet impacts the right interface of the bubble around time $t = 0.27$ μs, generating the propagation of an intense blast wave. Due to the short distance between the bubble and the wall, the rightward front wave impacts the wall and reflects at time $t = 0.28$ μs, leading to the most intense pressure peak on the wall (see Figure 8).

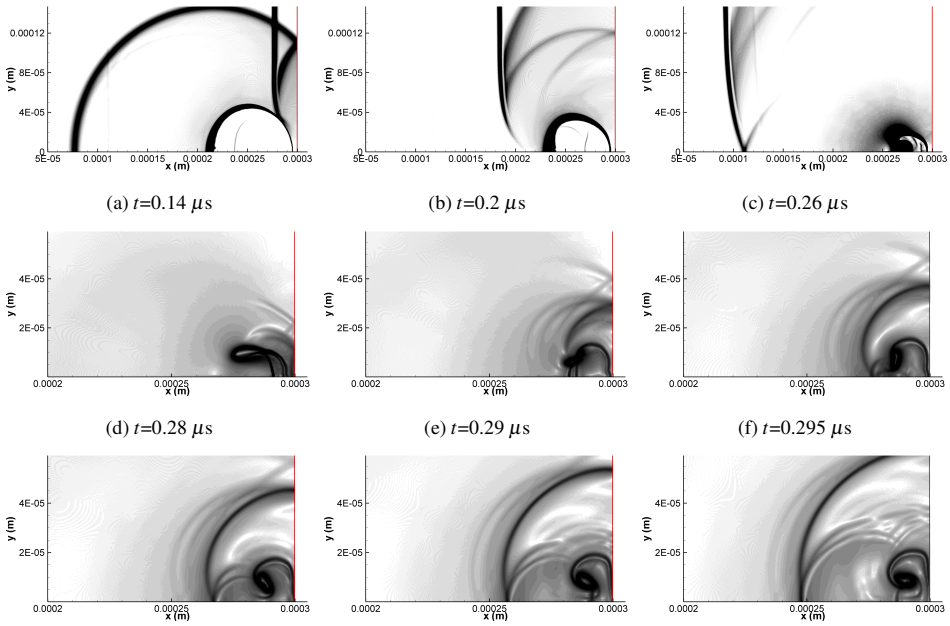

(a) t=0.14 μs (b) t=0.2 μs (c) t=0.26 μs

(d) t=0.28 μs (e) t=0.29 μs (f) t=0.295 μs

(g) t=0.3 μs (h) t=0.305 μs (i) t=0.31 μs

FIG. 7. Evolution of the density gradient for the 2D case $L/R_0 = 1.1$ at different times: a) t=0.14 μs, b) t=0.2 μs, c) t=0.26 μs, d) t=0.28 μs, e) t=0.29 μs, f) t=0.295 μs, g) t=0.3 μs, h) t=0.305 μs and i) t=0.31 μs.

At time $t = 0.29$ μs, we can see the leftward front of the blast wave followed by the reflected blast wave. These waves re-collapse the bubble pieces, generating another waves in the liquid. At time $t = 0.3$ μs, such a wave impacts the wall and reflects, leading to the third peak in the wall pressure evolution (see Figure 8). The reflected wave is well observed at time $t = 0.305$ μs and propagates more slowly due to the water velocity in the jet fluid (time $t = 0.31$ μs).

The maximum wall pressure reached during the collapse is plotted in Figure 8 (on the left). In comparison with the case $L/R = 2$, the third peak is clearly highlighted around time $t = 0.31$ μs. The axial velocity is plotted on the right part at different times. One can see that the high-speed water jet generated during the interaction reaches its maximum value (around 1100 m/s) around time t=0.28 μs when it collides with the right interface of the bubble.

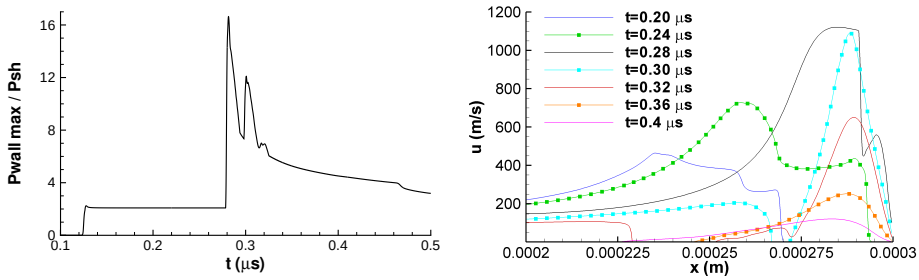

FIG. 8. Evolution for the case $L/R_0 = 1.1$ of: the maximum wall pressure reached during the collapse (left) and the longitudinal velocity along the symmetry axis (right).

C. Effects of the distance to the wall

We focus on the maximum wall pressure reached during the collapse, which corresponds to the impact of the water-hammer shock on the wall. The position of the bubble is varying from L/R_0=2 to 1.05. Results are compared with those obtained by Paquette et al. using a multicomponent model and the stiffened gas equation of state[34,53].

The time-evolution of the maximum wall pressure for different values of the stand-off distance L/R_0 is presented in Figure 9 (the left part). As expected, the closer the bubble is to the wall, the more intense the pressure peak is due to the water-hammer wave impact. Between the cases $L/R_0 = 1.9$ and $L/R_0 = 1.1$ the intensity of the pressure load is double. As the bubble moves closer to the wall the second pressure peak due to the impact of secondary waves increases and the moment of impact is gradually shifting.

The dimensionless maximum wall pressure P_{wmax}/P_{sh} is plotted in the same figure (the right part) as a function of the stand-off parameter L/R_0 and compared with the solution obtained by Paquette et al. We observe the same evolution: the wall pressure increases with the decrease of the stand-off distance. Yet, large discrepancies are noticeable on the pressure peak intensities obtained with both simulations, the gaps being more important when the stand-off distance decreases. It is certainly due to the behaviour of the multicomponent model used in the simulation as recently observed in the works of Goncalves and Parnaudeau[37] for an air-helium shock-bubble case. The pressure peaks and the bubble deformation obtained with the multicomponent model were under-predicted

in comparison with both the four-equation and the five-equation models.

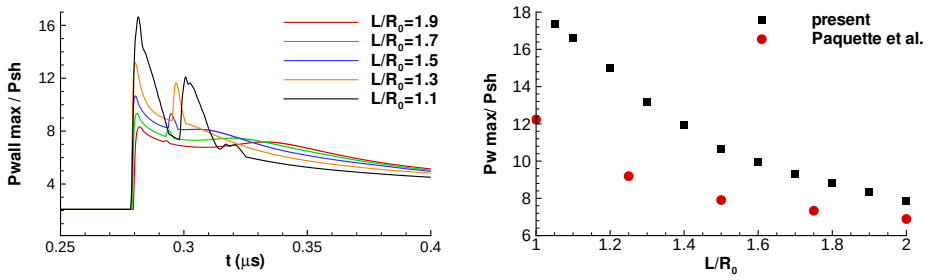

FIG. 9. Time-evolution of the maximum wall pressure (in bar) during the collapse for different values of L/R_0 (left) and evolution of the dimensionless maximum wall pressure with the parameter L/R_0 (right).

V. INVESTIGATION OF THE SPHERICAL BUBBLE COLLAPSE

Different 3D simulations have been performed by varying the stand-off distance similarly to the previous 2D study. All simulations were done using a constant time step $\Delta t = 10^{-11}$ s and the same grid with $N_r = 110$ as discussed in Section 3.

A. Case $L/R_0 = 2$

We consider the stand-off distance $L/R_0 = 2$. The main phenomena involved in the spherical case are similar to those described previously for the cylindrical case. The time-evolution of the dimensionless maximum pressure in the liquid (left part) and maximum pressure along the wall (right part) are illustrated in Figure 10. Pressures are divided by the incident post-shock pressure P_{sh}. The 2D result discussed previously is introduced for comparison. It is well known that the collapse process of a spherical bubble is faster and more intense in comparison with the cylindrical case. It is clearly illustrated on the maximum pressure in the fluid where a factor 3 is recorded for the most intense pressure peak with a time lag. The jet velocity reaches 1500 m/s instead of 800 m/s for the 2D case. Yet, as regard to the wall pressure, the peak intensity due to the water-hammer impact on the wall is quite similar between both simulations.

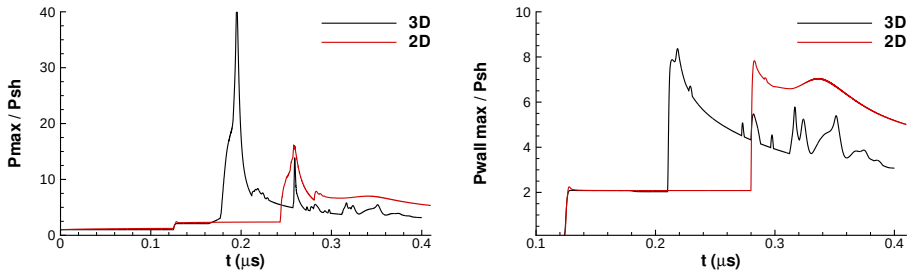

FIG. 10. Time-evolution of the dimensionless maximum pressure inside the fluid (left) and along the wall (right) for the stand-off distance $L/R_0 = 2$.

In order to evaluate the front velocity of the water-hammer wave propagating toward the wall, we plot in Figure 11 the isolines of the density gradient at different close times in the symmetry plane $x-z$. The rightward front velocity is around 1700 m/s. Similarly, the front velocity extracting from the 2D result is also around 1700 m/s, this explains why the peak pressures at the wall due the wave impact are quite identical. Therefore it seems that the wall pressure loads can be evaluated by using 2D simulations when the bubble is not too close to the wall.

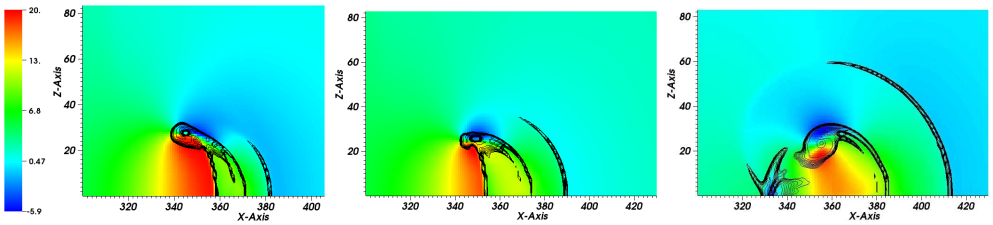

(a) $t = 0.182$ μs (b) $t = 0.185$ μs (c) $t = 0.195$ μs

FIG. 11. Dimensionless longitudinal velocity field u/u_{sh} and isolines of the density gradient at different times: a) $t = 0.182$ μs, b) $t = 0.185$ μs and c) $t = 0.195$ μs. Stand-off distance $L/R_0 = 2$.

The time evolution of the dimensionless effective bubble radius R/R_0 is plotted in Figure 12 (left part) and compared with the Keller-Miksis solution obtained with the initial pressure ratio $P_l/P_g = 1200$. The analytical profile is only given for illustrative purposes. The time is divided by the Rayleigh time t_R and, for the numerical solution, it is shifted to take into account the propagation of the incident shock wave toward the bubble (the time lag is computed with the

distance between the incident shock wave and the bubble interface divided by the speed of the front wave). Even if the bubble is no longer spherical, the volume decrease during the bubble contraction is close to the inertial free-field case up to the minimum radius around time $t/t_R = 1.2$. After this time, discrepancies appear on the rebound. The growth of the bubble follows the analytical profile on the beginning of the process but the first rebound is faster.

On the right part, the evolution of the maximum pressure inside the fluid (in GPa) is illustrated and compared with the Keller-Miksis solution. The strongest peak intensity of the numerical solution is quite similar to the theoretical value. A time lag is clearly highlighted for this peak: it occurs when the minimum volume is reached for the free-field collapse but it is not the case for the shock-induced collapse where the most intense pressure peak happens after the minimum volume has been attained. It is certainly due to the fact that the incident shock wave reflects on the wall and impacts the bubble during its contraction.

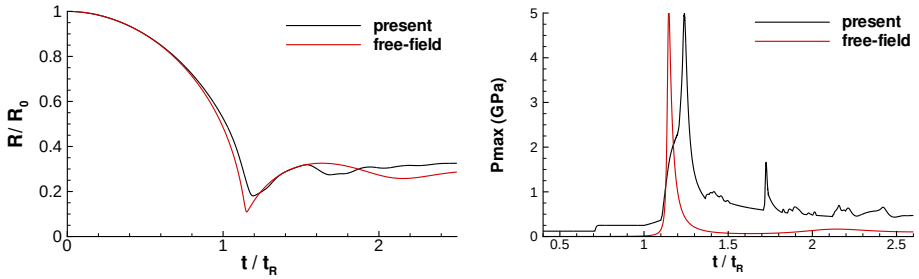

FIG. 12. Temporal evolution of the equivalent bubble radius R/R_0 (left) and the maximum pressure (in GPa) in the fluid (right) for the stand-off distance $L/R_0 = 2$.

To illustrate the collapse, visualizations at different times are plotted in Figure 13. Different quantities are presented on borders: the dimensionless longitudinal velocity component u/u_{sh} on the vertical symmetry plane, the dimensionless pressure on the wall P_w/P_{sh} and the modulus of the density gradient (Schlieren-like representation) on the horizontal symmetry plane. Inside the volume, the isosurface of void ratio $\alpha = 0.15$ is plotted. At time $t = 0.15$ μs, the incident shock wave has impacted the wall and the reflected wave is located near the right bubble interface. The bubble has a kidney shape due to the difference of pressure between both sides. At time $t = 0.18$ μs, the liquid jet is penetrating inside the bubble, leading to a toroidal shape and the reflected shock wave has impacted the bubble. Later, at time $t = 0.20$ μs the high-speed jet has impacted the

opposite bubble interface generating the spherical water-hammer shock. The longitudinal velocity of the jet reaches 1500 m/s. The toroidal shape of the bubble is clearly observed. The rightward front of the water-hammer shock impacts the wall causing an intense pressure peak and a reflected wave propagates toward the toroidal bubble ($t = 0.23$ μs). The reflected wave recollapses the bubble pieces around time $t = 0.25$ μs generating another pressure peak in the fluid, which can be seen in Figure 10. One can observe also the splitting of the toroidal bubble into two parts after time $t = 0.25$ μs. Multiple pressure waves are emitted during the recollapse process and impact the wall generating various pressure peaks at times $t = 0.30$ μs and 0.36 μs (see Figure 10). Later, at times $t = 0.45$ μs and 0.54 μs, the bubble attaches to the wall and spreads radially.

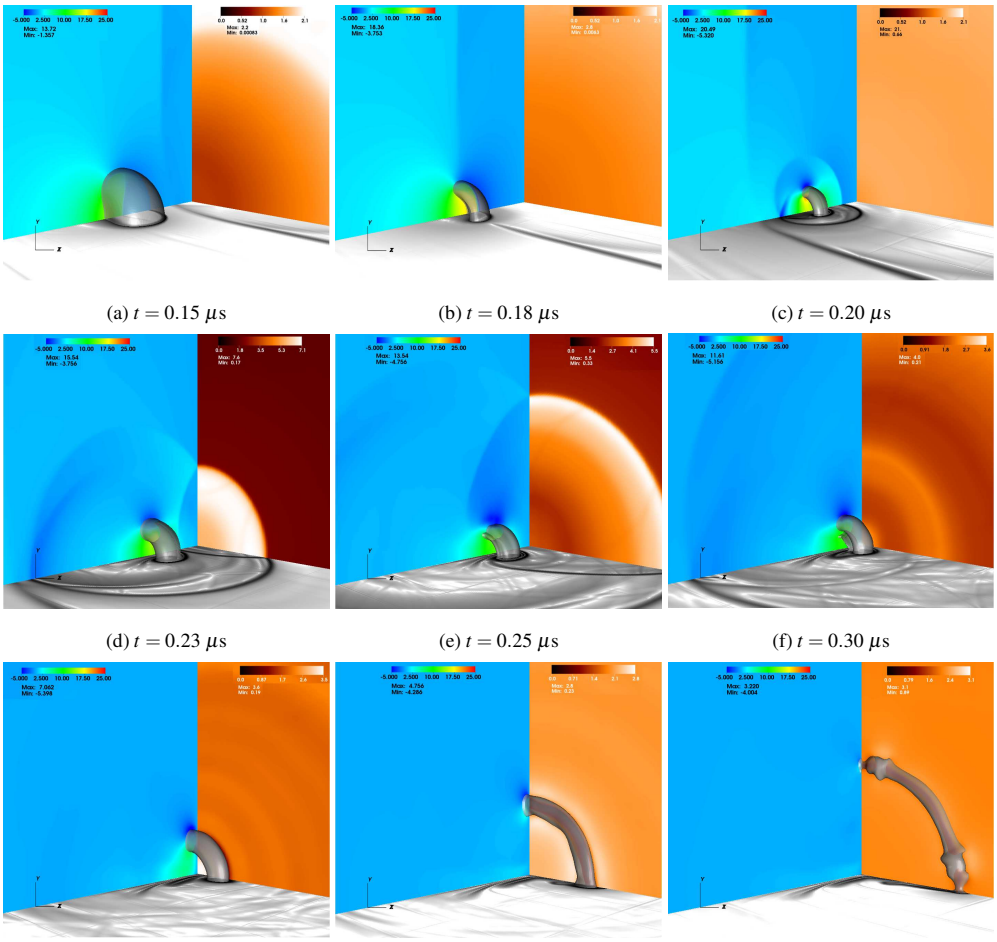

(a) $t = 0.15\ \mu$s (b) $t = 0.18\ \mu$s (c) $t = 0.20\ \mu$s

(d) $t = 0.23\ \mu$s (e) $t = 0.25\ \mu$s (f) $t = 0.30\ \mu$s

(g) $t = 0.36\ \mu$s (h) $t = 0.45\ \mu$s (i) $t = 0.54\ \mu$s

FIG. 13. Visualization of the 3D bubble collapse at different times for a stand-off distance $L/R_0 = 2$: a) $t = 0.15\ \mu$s, b) $t = 0.18\ \mu$s, c) $t = 0.20\ \mu$s, d) $t = 0.23\ \mu$s, e) $t = 0.25\ \mu$s, f) $t = 0.30\ \mu$s, g) $t = 0.36\ \mu$s, h) $t = 0.45\ \mu$s and i) $t = 0.54\ \mu$s. Dimensionless longitudinal velocity component u/u_{sh}, dimensionless wall pressure P/P_{sh}, Schlieren-like representation and iso-surface of void ratio $\alpha = 0.15$.

B. Case $L/R_0 = 1.4$

The bubble is now closer to the wall with a stand-off parameter $L/R_0 = 1.4$. The time-evolution of the dimensionless maximum pressure in the liquid (left part) and maximum pressure along the wall (right part) are illustrated in Figure 14. As expected the magnitude of the most intense peak due to the water-hammer formation is higher in 3D (by a factor 4) in comparison with the 2D simulation. The second peak due to the recollapse of bubble pieces by the reflected wave is pronounced with an intensity close to 24 times the incident post-shock pressure. At the wall the most intense pressure peak is stronger in 3D by a factor 2 in comparison with the cylindrical case. Different secondary peaks are illustrated due to the impact of multiple waves generated during the process.

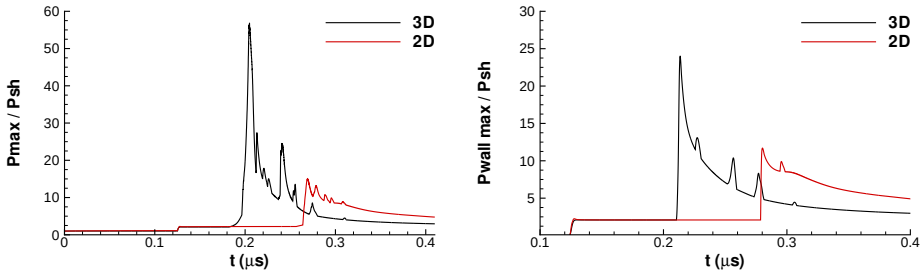

FIG. 14. Time-evolution of the dimensionless maximum pressure inside the fluid (left) and along the wall (right) for the stand-off distance $L/R_0 = 1.4$.

The time evolution of the dimensionless effective bubble radius R/R_0 is shown in Figure 15 (left part) and compared with the Keller-Miksis free-field solution. Similarly to the previous case, the time is shifted to take into account the travel of the incident shock wave to the bubble interface. The volume decrease matches particularly well the analytical profile until the minimum volume is reached. The rebound involves a succession of small oscillations and reaches a maximum volume value close to the analytical one. The maximum pressure peak plotted on the right part highlights a small time lag as commented previously. For this configuration where the bubble is relatively close to the wall, the peak intensity is higher than the analytical values.

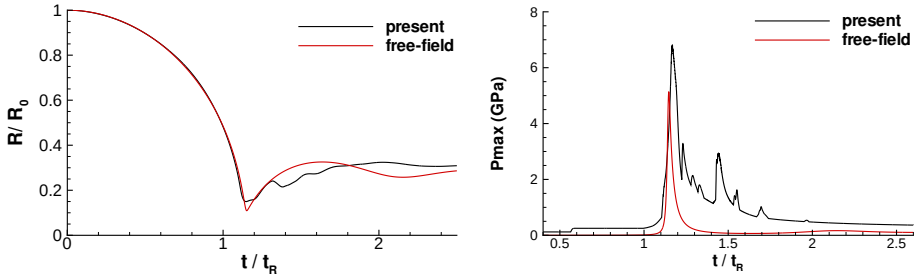

FIG. 15. Temporal evolution of the equivalent bubble radius R/R_0 (left) and the maximum pressure (in GPa) in the fluid (right) for the stand-off distance $L/R_0 = 1.4$.

Visualizations at different times are proposed in Figure 16 with the same quantities presented previously. A similar behaviour is observed with stronger phenomena. An enlargement is proposed for sub-figures b) to e) for a better view of the pressure waves. At time $t = 0.21$ μs the liquid jet piercing the bubble is close to reaching the opposite interface of the bubble, generating the water-hammer shock. This wave impacts the wall around time $t = 0.22$ μs causing the most intense wall pressure peak. At time $t = 0.23$ μs, the reflected wave due to the impact of the water-hammer shock on the wall is close to recollapsing the toroidal bubble. A series of pressure waves propagates upstream in front of the torus due to multiple interactions and reflexions. The rarefaction wave generated when the incident shock collides with the left bubble interface impacts the wall and reflects (see Figure 6b) for the 2D case). Moreover, this reflected wave and the reflected shock wave due to the impact of the incident shock collide with the right interface of the bubble, leading to new waves (see Figure 6c) for the 2D case), which reflect on the wall. At time $t = 0.26$ μs, the reflected water-hammer shock has recollapsed the bubble and the splitting of the toroidal bubble after the wave impact is well illustrated at time $t = 0.28$ μs. Multiple waves are emitted and intersect together leading to a complex network of waves. At times $t = 0.39$ μs and $t = 0.48$ μs the toroidal bubble spreads along the wall.

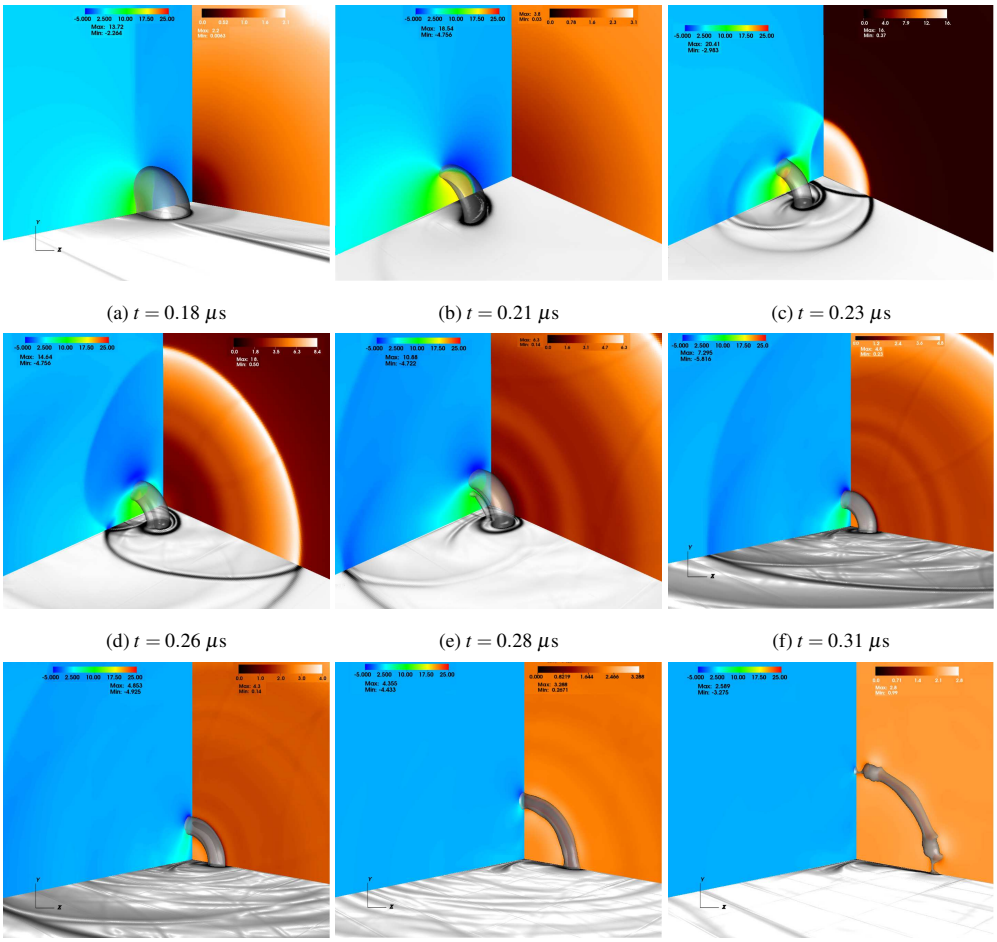

(a) $t = 0.18\ \mu$s (b) $t = 0.21\ \mu$s (c) $t = 0.23\ \mu$s

(d) $t = 0.26\ \mu$s (e) $t = 0.28\ \mu$s (f) $t = 0.31\ \mu$s

(g) $t = 0.33\ \mu$s (h) $t = 0.39\ \mu$s (i) $t = 0.48\ \mu$s

FIG. 16. Visualization of the 3D bubble collapse at different times for a stand-off distance $L/R_0 = 1.4$: a) $t = 0.18\ \mu$s, b) $t = 0.21\ \mu$s, c) $t = 0.23\ \mu$s, d) $t = 0.26\ \mu$s, e) $t = 0.28\ \mu$s, f) $t = 0.31\ \mu$s, g) $t = 0.33\ \mu$s, h) $t = 0.39\ \mu$s and i) $t = 0.48\ \mu$s. Dimensionless longitudinal velocity component u/u_{sh}, dimensionless wall pressure P/P_{sh}, Schlieren-like representation and iso-surface of void ratio $\alpha = 0.15$.

C. Case $L/R_0 = 1.1$

Let's consider now the case where the bubble is very close to the wall with a stand-off distance $L/R_0 = 1.1$. The time-evolution of the dimensionless maximum pressure in the liquid (left part) and maximum pressure along the wall (right part) are shown in Figure 17. The intensity of pressure peaks obtained with the 3D simulation is huge and highlights the differences with the 2D result. Inside the fluid, the maximum pressure peak is around 105 times the incident post-shock pressure and around 7 times the 2D peak (that is a difference of 600%). Moreover, a different behaviour is observed for the second peak due to the recollapse of the bubble. For the 2D cylindrical case, the second peak is higher than the first one (see Figure 5 in Section 3). It is not the case for the spherical collapse where the intensity of the second peak is around 3.5 times weaker than the first peak. At the wall, due the proximity of the bubble, the intensity of the pressure peaks is close to the intensity of the peaks inside the fluid. In comparison with the 2D simulation, a factor 7 is illustrated for the strongest peak intensity. The evaluation of pressure loads on the wall using 2D simulations is therefore questionable for such a configuration.

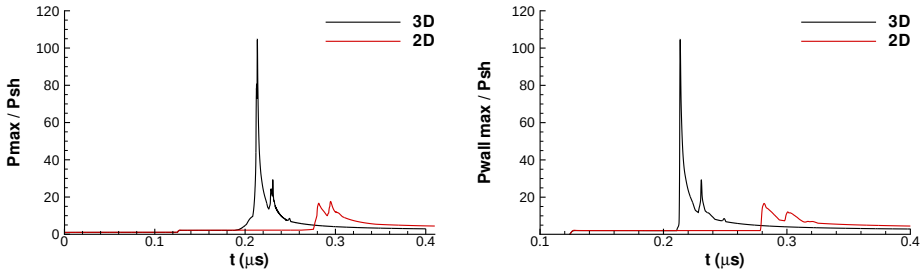

FIG. 17. Time-evolution of the dimensionless maximum pressure inside the fluid (left) and along the wall (right) for the stand-off distance $L/R_0 = 1.1$.

The time evolution of the dimensionless effective bubble radius R/R_0 is plotted in Figure 18 (left part) and compared with the free-field solution. Similarly to the previous configurations, the volume decrease perfectly fits the analytical profile until the minimum volume is reached. Moreover, the rebound is very close to the analytical evolution. One can observe an undulation between time $t/t_R = 1.15$ and $t/T_R = 1.22$ close to the minimum value before the growth of the volume, certainly due to the impact of a reflected wave emanating from the wall. For the maximum

pressure peak illustrated on the right part, a similar comment to the previous cases can be drawn with the existence of a small time lag and a stronger intensity due to the short distance to the wall.

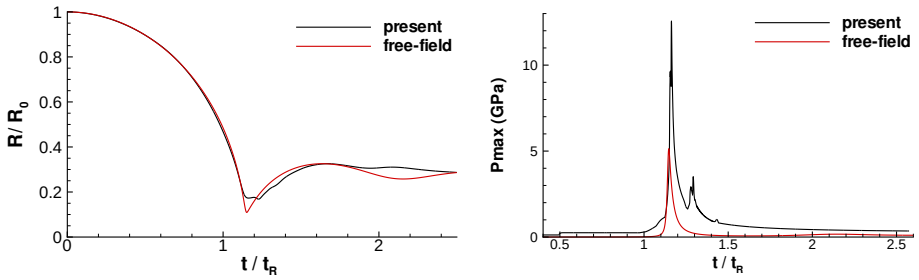

FIG. 18. Temporal evolution of the equivalent bubble radius R/R_0 (left) and the maximum pressure (in GPa) in the fluid (right) for the stand-off distance $L/R_0 = 1.1$.

Visualizations at different times are illustrated in Figure 19. An enlargement is proposed for sub-figures c) to f) for a better view of the pressure waves. Due to the proximity of the bubble with the wall, the dynamics is very fast and strong. The longitudinal velocity of the liquid jet reaches 2000 m/s. At time $t = 0.225$ μs, the water-hammer shock has impacted the wall leading to the most intense wall pressure peak and the reflected wave is close to recollapsing the toroidal bubble. The leftward front of the water hammer shock can be observed inside the torus. At time $t = 0.23$ μs, the reflected water-hammer shock has recollapsed the toroidal bubble leading to another pressure peak. A secondary wave inside the torus and propagating upstream is clearly illustrated at time $t = 0.24$ μs. The bubble attaches to the wall at time $t = 0.28$ μs and spreads laterally.

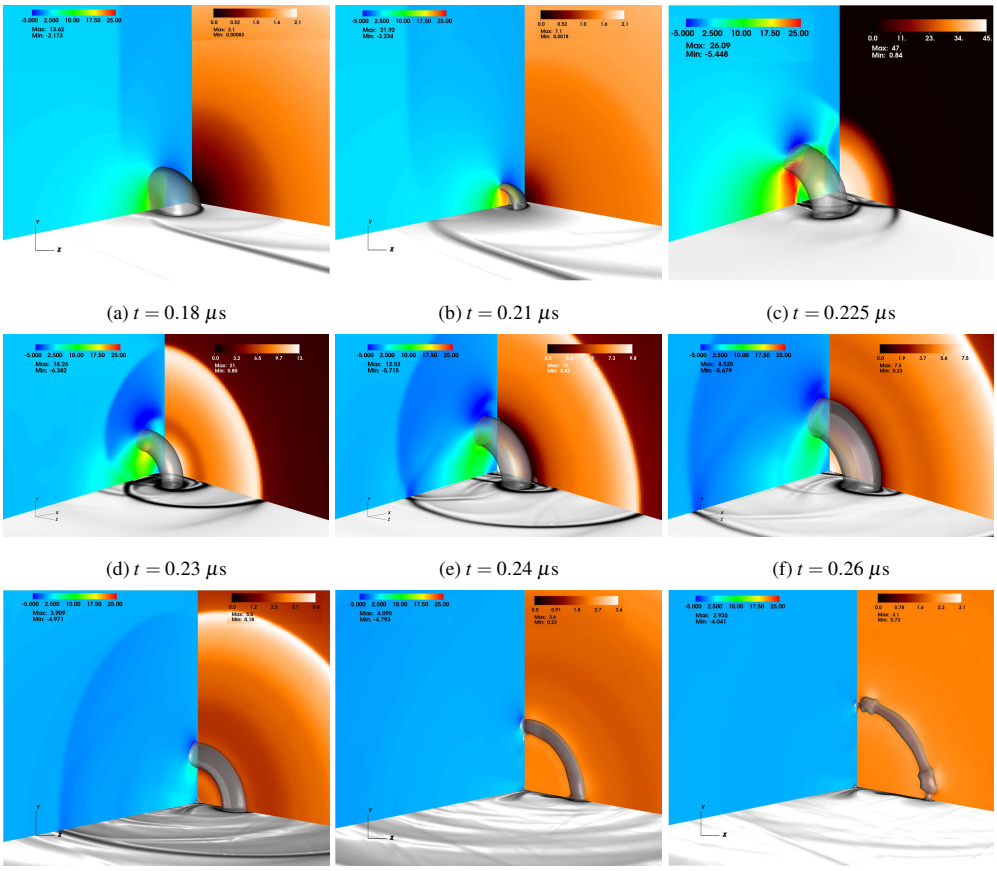

(a) $t = 0.18\ \mu$s (b) $t = 0.21\ \mu$s (c) $t = 0.225\ \mu$s

(d) $t = 0.23\ \mu$s (e) $t = 0.24\ \mu$s (f) $t = 0.26\ \mu$s

(g) $t = 0.28\ \mu$s (h) $t = 0.33\ \mu$s (i) $t = 0.38\ \mu$s

FIG. 19. Visualization of the 3D bubble collapse at different times for a stand-off distance $L/R_0 = 1.1$: a) $t = 0.18\ \mu$s, b) $t = 0.21\ \mu$s, c) $t = 0.225\ \mu$s, d) $t = 0.23\ \mu$s, e) $t = 0.24\ \mu$s, f) $t = 0.26\ \mu$s, g) $t = 0.28\ \mu$s, h) $t = 0.33\ \mu$s and i) $t = 0.38\ \mu$s. Dimensionless longitudinal velocity component u/u_{sh}, dimensionless wall pressure P/P_{sh}, Schlieren-like representation and iso-surface of void ratio $\alpha = 0.15$.

D. Effects of the distance to the wall

Similarly to the cylindrical case, we focus on the maximum pressure along the wall reached during the collapse. The stand-off distance is varying from $L/R_0 = 2$ to 1.1. Results are also

compared with the previous 2D simulations.

Based on the previous analyses for all considered stand-off distances, it is shown that the highest pressure at the wall is induced by the impact of the water-hammer shock wave emitted during the collapse. This result is corroborated by the recent experimental study of Dular et al.[39]. Moreover, by comparing the evolution for the wall pressure of the maximum value and the axis value (not presented here), it is attested that the highest pressures occur on the axis of the bubble.

The time-evolution of the maximum wall pressure is plotted in Figure 20 for different values of the stand-off distance from 2 to 1.2. The pressure load obtained with $L/R_0 = 1.1$ is so huge that the pressure evolution is plotted alone in the right part of the figure. As observed for the cylindrical case, the most intense peak increases when the bubble moves toward the wall. For the stand-off distance $L/R_0 = 1.1$, the pressure peak is extremely strong (around 120,000 bar) and is 12 times the peak value observed for $L/R_0 = 2$. Other small peaks appearing after the water-hammer shock impact correspond to secondary waves generated by the recollapse of the bubble pieces and impacting the wall.

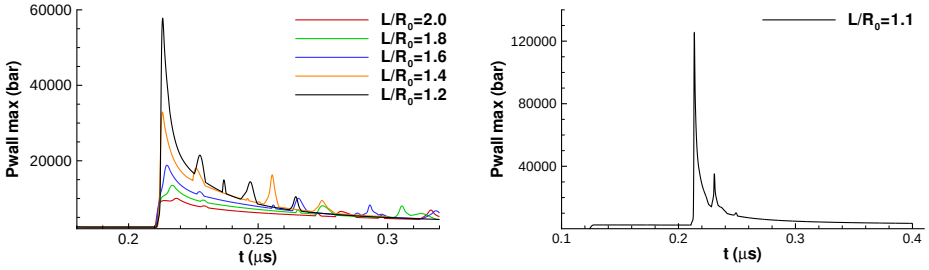

FIG. 20. Time evolution of the maximum wall pressure (in bar) for different values of the stand-off parameter L/R_0: from 2 to 1.2 (left) and for L/R_0=1.1 (right).

The comparison with 2D simulations is illustrated in Figure 21 where is plotted the dimensionless maximum wall pressure P_w/P_{sh} as a function of the stand-off distance (left part). As previously commented, the highest wall pressure obtained with a 2D simulation is fairly close to the 3D solution when the stand-off distance $L/R_0 > 1.8$ (the gap is about 7% for $L/R_0 = 2$) . It is no more the case as the bubble approaches the wall. The gap between 3D and 2D results signif-

icantly increases when the stand-off parameter decreases. It is double for $L/R_0 = 1.4$, triple for $L/R_0 = 1.2$, it differs by a factor of 7 for $L/R_0 = 1.1$ and almost by a factor of 9 for $L/R_0 = 1.05$.

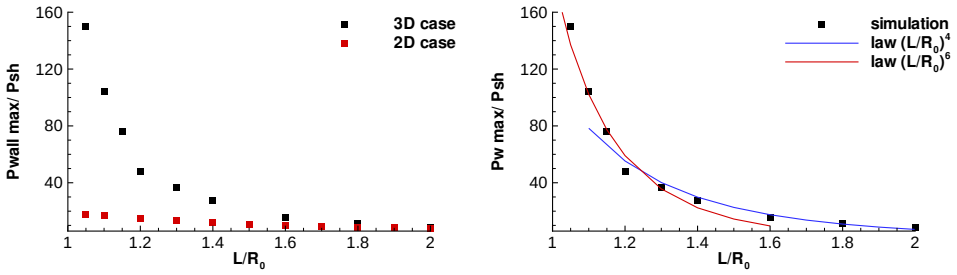

FIG. 21. Evolution of the dimensionless maximum wall pressure P_w/P_{sh} with the stand-off parameter L/R_0. Comparison between 3D and 2D simulations (left) and law for the 3D collapse (right).

On the right part of the same figure, we propose two power-laws fitting the evolution of the maximum wall pressure as a function of the stand-off distance. The maximum value of the wall pressure is of primary interest when estimating the material damage. A pit can form on the material surface when the wall pressure is large enough to result in high equivalent stresses that exceed the local material yield stress. Different authors have proposed to model the magnitude of pressure peaks involved in a bubble collapse. We can cite the works of Vogel and Lauterborn[20] and the works of Johnsen and Colonius[7] for which the wall pressure formulation involves two parameters that can be determined if two pressure measurements are known. Brujan et al.[54] proposed a formulation based on the equation of state of Rice and Walsh. Recently, Supponen et al.[10]proposed an empirical model for predicting the shock strengths for nonspherical bubbles by exploiting a large number of data. This law is well suited for collapses induced by a driving pressure and not for strong shock-induced collapse.

Our formulation is based on power laws of the type

$$\frac{P_{wall\,max}}{P_{sh}} = \frac{C}{(L/R_0)^p} \tag{18}$$

with a constant C and an exponent p.

When the bubble is not too close to the wall, the law with $p = 4$ shows a very good agreement with the numerical results. When the bubble is close to attach the wall (from $L/R_0 = 1.2$), the law with $p = 6$ scales very well the data.

For an illustrative purpose, four configurations for which the bubble is initially attached to the wall have been computed ($\Gamma < 1$). The dimensionless maximum pressure on the wall is given in Table I when the stand-off distance varies between 0.95 and 0.7. A non-monotonic behaviour is illustrated with a large diminuation of the peak in comparison with the stand-off distance $1 < \Gamma < 1.15$ and a growing intensity when $\Gamma < 0.8$, as observed in the experimental study of Shima et al.[13].

	STAND-OFF DISTANCE L/R_0			
	0.95	0.9	0.8	0.7
maximum wall pressure $P_{wall\,max}/P_{sh}$	53.8	67.0	65.5	78.5

TABLE I. Dimensionless maximum wall pressure for different values of the stand-off distance $L/R_0 < 1$ corresponding to an attached bubble.

VI. INVESTIGATION OF A TWIN-BUBBLE COLLAPSE

The interdependence of bubbles and the possible intensification of the peak pressure has been discussed by different authors[26,42,55]. We present a simple configuration with only two bubbles of equal size. This test is an extension of the previous one by considering a second bubble placed behind the first bubble. We introduce the dimensionless distance S/R_0 between the bubbles' centers. Different configurations are simulated by varying the inter-bubble distance from 2.5 to 5. The stand-off distance is set to 2. We focus on the possible increase of the wall pressure in comparison with the single-bubble configuration with the same stand-off distance. Numerical parameters are similar to the previous case.

Visualizations of the collapse for the inter-bubble distance $S/R_0 = 3$ are illustrated in Figure 22. For the first bubble, the collapse is similar to the single-bubble case. As shown by Lauer et al.[26], the second bubble collapse follows the same process for which the water-hammer shock emitted by the first collapse plays the role of the incident shock. At time $t = 0.20\ \mu$s, the water-hammer shock generated by the collapse of the first bubble propagates toward the second bubble and the incident shock has already impacted the second bubble leading to the beginning of its contraction. At time $t = 0.25\ \mu$s, the water-hammer shock emitted by the first collapse has impacted the second bubble and the incident shock has impacted the wall leading to a first peak pressure (see Figure 24). The

water-hammer shock emitted by the first bubble collapse impacts the wall around time $t = 0.30$ μs and, at the same time, the second bubble collapse generates another water-hammer shock. At time $t = 0.31$ μs, one can observe on the contours of density gradient two shock fronts travelling towards the wall: the water-hammer front followed by a secondary wave. These two shocks are clearly highlighted in 2D results for the inter-bubble distance $S/R_0 = 4$, as shown in Figure 23 where contours of the density gradient are plotted at different times. Secondary shocks are emitted during the first bubble collapse after the generation of the water hammer shock. When the leftward water-hammer front impacts the bubbles pieces, it compresses the gas inside the lobes forming shock waves. These shocks interact with the water-hammer shock and with themselves. In the right figure, the two fronts travelling toward the second bubble are well illustrated.

At the wall, in Figure 22, a succession of wave impacts leads to the generation of pressure loads: the impact of the first water-hammer shock at time $t = 0.31$ μs (22e), then the impact of the second water-hammer shock at time $t = 0.32$ μs (22f) leading to the most intense pressure peak (see next figure) and the secondary wave discussed previously around time $t = 0.328$ μs. Inside the fluid, around time $t = 0.34$ μs, the reflected wave due to the impact on the wall of the first water-hammer shock causes the recollapse of the second bubble pieces and the leftward front of the second water-hammer shock causes the recollapse of the first bubble fragments. Later, the multiple waves continue their propagation and the second bubble attaches to the wall.

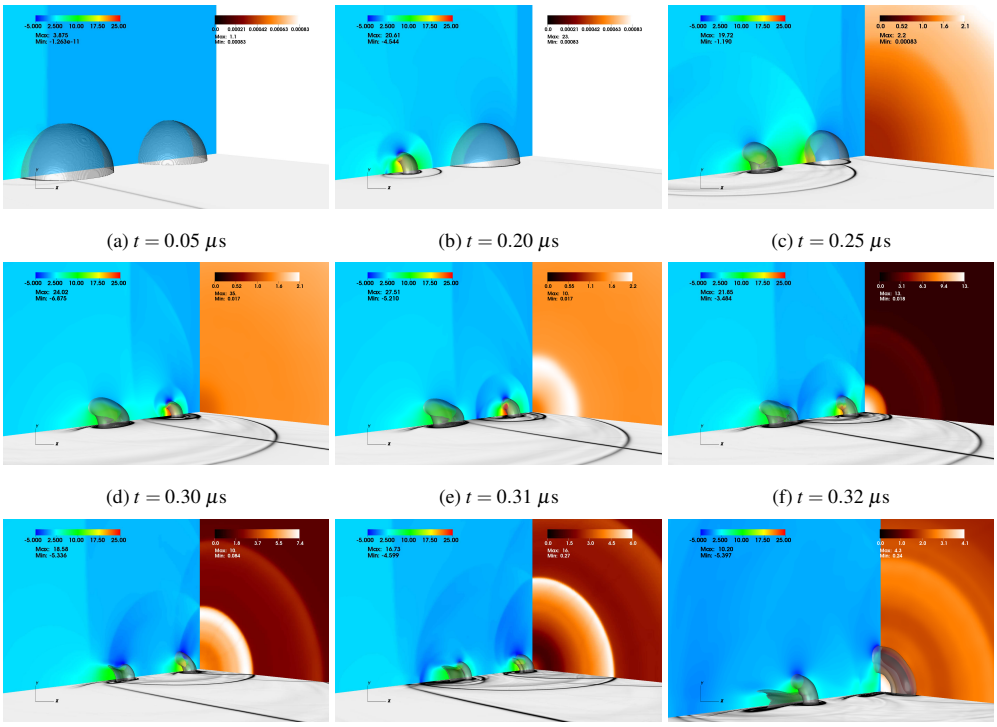

(a) $t = 0.05\ \mu$s (b) $t = 0.20\ \mu$s (c) $t = 0.25\ \mu$s

(d) $t = 0.30\ \mu$s (e) $t = 0.31\ \mu$s (f) $t = 0.32\ \mu$s

(g) $t = 0.34\ \mu$s (h) $t = 0.36\ \mu$s (i) $t = 0.45\ \mu$s

FIG. 22. Visualization of the twin-bubble collapse at different times for an inter-bubble distance $S/R_0 = 3$ and a stand-off distance $L/R_0 = 2$: a) $t = 0.05\ \mu$s, b) $t = 0.20\ \mu$s, c) $t = 0.25\ \mu$s, d) $t = 0.30\ \mu$s, e) $t = 0.31\ \mu$s, f) $t = 0.32\ \mu$s, g) $t = 0.34\ \mu$s, h) $t = 0.36\ \mu$s and i) $t = 0.45\ \mu$s. Dimensionless longitudinal velocity component u/u_{sh}, dimensionless wall pressure P/P_{sh}, Schlieren-like representation and iso-surface of void ratio $\alpha = 0.15$.

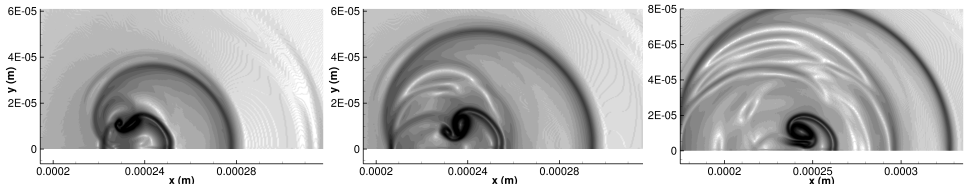

FIG. 23. Contours of the density gradient at three close moments. 2D simulation with an inter-bubble distance $S/R_0 = 4$ and a stand-off distance $L/R_0 = 2$.

The same main phenomena are involved for the configurations with $S/R_0 = 2.5$, 4 and 5. They are not presented here. According to the inter-bubble distance, the two consecutive shocks discussed above can merge together forming a much stronger shock before impacting the wall.

The intensification of the second bubble collapse relative to the first one is illustrated in Figure 24 where the evolution of the dimensionless maximum pressures on the wall and inside the fluid are plotted. Due to the low pressure region between consecutive bubbles, the maximum pressure after the collapse of the first one (around time $t = 0.20$ μs) does not reach the maximum pressure of the single-bubble case. For the configuration $S/R_0 = 2.5$, expansion waves largely decrease the maximum pressure during the collapse of the first bubble (around 60%). In all cases, the water-hammer shock emitted during the first collapse is much stronger than the incident shock leading to an amplification of the maximum pressure in the fluid during the second collapse. In regard to the influence of the inter-bubble distance, a non-monotonic behaviour is observed and the highest peak intensity in the fluid is obtained for the distance $S/R_0 = 3$, the maximum value being the double of the first peak intensity. At the wall, the maximum wall pressure computed for all configurations is more intense in comparison with the single-bubble collapse. The amplification rate reaches approximatively 50% for all cases. The wall pressure signals present a double peak corresponding to the impact of the water-hammer shock emitted by the second bubble collapse and followed by the impact of the secondary wave discussed previously. For the distance $S/R_0 = 2.5$, a third intense peak is highlighted around time $t = 0.37$ μs due to the impact of the pressure wave generated by the recollapse of the second bubble pieces.

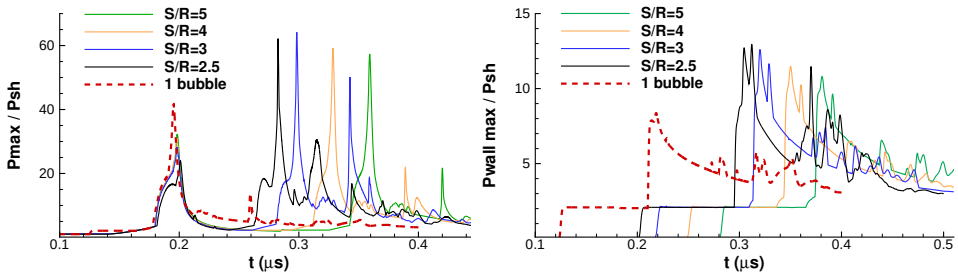

FIG. 24. Time-evolution of the dimensionless maximum pressure inside the fluid (left) and along the wall (right) for different inter-bubble distances and for a stand-off distance $L/R_0 = 2$.

VII. CONCLUSION

In the present study, a numerical investigation of a shock-induced bubble collapse and the potential damage for the wall located in the vicinity of the bubble is proposed. Simulations are performed using an efficient parallel compressible two-phase solver based on a four-equation model. The importance of the divergence term appearing in the void ratio transport equation is illustrated. It is also shown that viscous effects can be neglected for such configurations.

The mechanism inducing the highest wall pressure peaks in the domain and at the wall are described when the stand-off distance varies for both the cylindrical and spherical cases. The most intense pressure peak at the wall is generated by the impact of the water-hammer shock emitted during the collapse. For the stand-off distance $\Gamma = 1.1$, the wall pressure peak is extremely strong and is 100 times the intensity of the incident shock wave. This pressure loading can cause high stresses inside the material making the structure more vulnerable of having micro-ruptures. The evolution of the highest pressure peak as a function of the stand-off distance is analyzed. A power-law is proposed with a very good agreement with the obtained numerical data. Such a law can feed an empirical erosion criterion to evaluate the material damage and to predict the zone where plasticity will occur. The wall loads can also be expressed in terms of an erosion probability. Comparisons with the analytical solution of the free-field collapse show that the volume decrease perfectly follows the analytical solution. Moreover, the results underlines the importance of performing 3D simulations for the prediction of the pressure loads in comparison with 2D results when the bubble approaches the wall. The gap between 2D and 3D results on the wall pressure reaches 600% for the stand-off distance $\Gamma = 1.1$.

Finally a twin-bubble collapse is investigated to evaluate the collective effects and the potential for achieving a significant increase of the wall pressure levels. A parametric study was performed by varying the inter-bubble distance for a fixed stand-off distance. Results highlight the possible intensification of the wall pressure peak around 50% in comparison with the single-bubble configuration, which can induce significant material damage.

Ongoing and future works are in progress to better understand and to predict cavitation erosion. Different directions will be investigated: i) to compute other single-bubble cases to test the proposed law for the maximum wall pressure, ii) to investigate multi-bubble collapse for different bubbles arrangement, iii) to link the characteristic erosion pattern to the local flow field obtained with CFD simulations and iv) to perform fluid-structure coupled simulations that incorporate suit-

able material models.

ACKNOWLEDGMENTS

This research was supported by the French National Research Agency ANR (project 18-CE46-009). Computations have been performed on the supercomputer facilities of the Mesocentre CRIANN (project 2018004) and the HPC resources of GENCI under allocations A0072A10981.

Data Availability

The data that support the findings of this study are available from the corresponding author upon reasonable request.

Author contributions

All of the authors were involved in the preparation of the manuscript and have read and approved the final manuscript version.

REFERENCES

[1]A. Jamaluddin, G. Ball, C. Turangan, and T. Leighton, "The collapse of single bubbles and approximation of the far-field acoustic emissions for cavitation induced by shock wave lithotripsy," Journal of Fluid Mechanics **677**, 305–341 (2011).

[2]C.-D. Ohl, M. Arora, R. Dijkink, V. Janve, and D. Lohse, "Surface cleaning from laser-induced cavitation bubbles," Applied Physics Letters **89**, 074102 (2006).

[3]M. Plesset and R. Chapman, "Collapse of an initially spherical vapour cavity in the neighbourhood of a solid boundary," Journal of Fluids Mechanics **47**, 283–290 (1971).

[4]J. Haas and B. Sturtevant, "Interaction of weak shock waves with cylindrical and spherical gas inhomogeneities," Journal of Fluid Mechanics **181**, 41–76 (1987).

[5]N. Bourne, "On the collapse of cavities," Shock Waves **11**, 447–455 (2002).

[6]C. Turangan, A. Jamaluddin, G. Ball, and T. Leighton, "Free-lagrange simulations of the expansion and jetting collapse of air bubbles in water," Journal of Fluid Mechanics **598**, 1–25 (2008).

[7]E. Johnsen and T. Colonius, "Numerical simulations of non-spherical bubble collapse," Journal of Fluid Mechanics **629**, 231–262 (2009).

[8]N. Hawker and Y. Ventikos, "Interaction of a strong shockwave with a gas bubble in a liquid mediam: a numerical study," Journal of Fluid Mechanics **701**, 59–97 (2012).

[9]M. Ozlem, D. Schwendeman, A. Kapila, and W. Henshaw, "A numerical study of shock-induced cavity collapse," Shock Waves **22**, 89–117 (2012).

[10]O. Supponen, D. Obreschkow, P. Kobel, M. Tinguely, N. Dorsaz, and M. Farhat, "Shock waves from nonspherical cavitation bubbles," Physical Review Fluids **2**, 093601 (2017).

[11]Y. Tomita and A. Shima, "Mechanisms of impulsive pressure generation and damage pit formation by bubble collapse," Journal of Fluid Mechanics **169**, 535–564 (1986).

[12]A. Philipp and W. Lauterborn, "Cavitation erosion by single laser-produced bubbles," J. Fluid Mechanics **361**, 75–116 (1998).

[13]A. Shima, K. takayama, Y. Tomita, and N. Ohsawa, "Mechanism of impact pressure generation from spark-generated bubble collapse near a wall," AIAA Journal **21**, 55–59 (1983).

[14]J. Blake, Y. Tomita, and R. Tong, "The art, craft and science of modelling jet impact in a collapsing cavitation bubble," In Fascination of Fluid Dynamics. Springer (1998).

[15]R. Tong, W. Schiffers, S. Shaw, J. Blake, and D. Emmony, "The role of 'splashing' in the collapse of a laser-generated cavity near a rigid boundary," Journal of Fluid Mechanics **380**, 339–361 (1999).

[16]C.-T. Hsiao, A. Jayaprakash, A. Kapahi, J.-K. Choi, and G. Chahine, "Modeling of material pitting from cavitation bubble collapse," Journal of Fluid Mechanics **755**, 142–175 (2014).

[17]J. Choi and G. Chahine, "Relationship between material pitting and cavitation field impulsive pressures," Wear **352**, 42–53 (2016).

[18]C. Turangan, G. Ball, A. Jamaluddin, and T. Leighton, "Numerical studies of cavitation erosion on an elastic–plastic material caused by shock-induced bubble collapse," Proc. Royal Society A **473**, 20170315 (2017).

[19]S. Joshi, J.-P. Franc, G. Ghigliotti, and M. Fivel, "SPH modelling of a cavitation bubble collapse near an elasto-visco-plastic material," Journal of the Mechanics and Physics of Solids **125**, 420–439 (2019).

[20]A. Vogel and W. Lauterborn, "Acoustic transient generation by laser-produced cavitation bubbles near solid boundaries," The Journal of the Acoustical Society of America **84**, 719–731 (1988).

[21]S. Gonzalez-Avila, F. Denner, and C.-D. Ohl, "The acoustic pressure generated by the cavitation bubble expansion and collapse near a rigid wall," Physics of Fluids **33**, 032118 (2021).

[22]G. Ball, B. Howell, T. Leighton, and M. Schofield, "Shock-induced collapse of a cylindrical air cavity in water: a Free-Lagrange simulation," Shock Waves **10**, 265–276 (2000).

[23]H. Terashima and G. Tryggvason, "A front-tracking/ghost-fluid method for fluid interfaces in compressible flows," Journal of Computational Physics **228**, 4012–4037 (2009).

[24]X. Hu, B. Khoo, N. Adams, and F. Huang, "A conservative interface method for compressible flow," Journal of Computational Physics **219**, 553–578 (2006).

[25]R. Nourgaliev, T. Dinh, and T. Theofanous, "Adaptive characteristics-based matching for compressible multifluid dynamics," Journal of Computational Physics **213**, 500–529 (2006).

[26]E. Lauer, X. Hu, S. Hickel, and N. Adams, "Numerical investigation of collapsing cavity arrays," Physics of Fluids **24**, 052104 (2012).

[27]G. Allaire, S. Clerc, and S. Kokh, "A five-equation model for the simulation of interfaces between compressible fluids," Journal of Computational Physics **181**, 577–616 (2002).

[28]K. Shyue, "A volume-fraction based algorithm for hybrid barotropic and non-barotropic two-fluid flow problems," Shock Waves **15**, 407–423 (2006).

[29]V. Coralic and T. Colonius, "Shock-induced collapse of a bubble inside a deformable vessel," European Journal of Mechanics B/Fluids **40**, 64–74 (2013).

[30]Y.-L. Yoo and H.-G. Sung, "Numerical investigation of an interaction between shock waves and bubble in a compressible multiphase flow using a diffuse interface method," International Journal of Heat and Mass Transfer **127**, 210–221 (2018).

[31]F. Denner and B. van Wachem, "Numerical modelling of shock-bubble interactions using a pressure-based algorithm without Riemann solvers," Experimental and Computational Multiphase Flow **1**, 274–285 (2019).

[32]E. Klaseboer, S. Fong, C. Turangan, B. Khoo, A. Szeri, M. Calvisi, G. Sankin, and P. Zhong, "Interaction of lithotripter shockwaves with single inertial cavitation bubbles," Journal of Fluid Mechanics **593**, 33–56 (2007).

[33]R. Han, L. Tao, A.-M. Zhang, and S. Li, "A three-dimensional modeling for coalescence of multiple cavitation bubbles near a rigid wall," Physics of fluids **31**, 062107 (2019).

[34]S. Beig and E. Johnsen, "Maintaining interface equilibrium conditions in compressible multiphase flows using interface capturing," Journal of Computational Physics **302**, 548–566 (2015).

[35]F. Wermelinger, U. Rasthofer, P. Hadjidoukas, and P. Koumoutsakos, "Petascale simulations of compressible flows with interfaces," J. Computational Science **26**, 217–225 (2018).

[36]N. Bempedelis and Y. Ventikos, "Energy focusing in shock-collapsed bubble arrays," Journal of Fluid Mechanics **900**, A44 (2020).

[37]E. Goncalves and P. Parnaudeau, "Comparison of multiphase models for computing shock-induced bubble collapse," International Journal of Numerical Methods for Heat and Fluid Flow **30**, 3845–3877 (2020).

[38]T. Trummler, S. Schmidt, and N. Adams, "Effect of stand-off distance and spatial resolution on the pressure impact of near-wall vapor bubble collapses," International Journal of Multiphase Flow **141**, 103618 (2021).

[39]M. Dular, T. Pozar, J. Zevnik, and R. Petkovsek, "High speed observation of damage created by a collapse of a single cavitation bubble," Wear **418-419**, 13–23 (2019).

[40]E. Goncalves and D. Zeidan, "Simulation of compressible two-phase flows using a void ratio transport equation," Communication in Computational Physics **24**, 167–203 (2018).

[41]S. Mottyll and R. Skoda, "Numerical 3d flow simulation of ultrasonic horns with attached cavitation structures and assessment of flow aggressiveness and cavitation erosion sensitive wall zones," Ultrasonics Sonochemistry **31**, 570–589 (2016).

[42]M. Betney, B. Tully, N. Hawker, and Y. Ventikos, "Computational modelling of the interaction of shock waves with multiple gas-filled bubbles in a liquid," Physics of Fluids **27**, 036101 (2015).

[43]E. Goncalves and B. Charriere, "Modelling for isothermal cavitation with a four-equation model," International Journal of Multiphase Flow **59**, 54–72 (2014).

[44]A. Tiwari, J. Freund, and C. Pantano, "A diffuse interface model with immiscibility preservation," Journal of Computational Physics **252**, 290–309 (2013).

[45]G. Wallis, "One-dimensional two-phase flow," New York: McGraw-Hill (1967).

[46]C. Ishii and T. Hibiki, "Thermo-fluid dynamics of two-phase flow," Springer (2006).

[47]E. Toro, M. Spruce, and W. Speares, "Restoration of the contact surface in the HLL-Riemann solver," Shock Waves **4**, 25–34 (1994).

[48]B. van Leer, "On the relation between the upwind-differencing schemes of Godunov, Engquist-Osher and Roe," SIAM Journal on Scientific and Statistical Computing **5**, 1–20 (1984).

[49]R. Dubois, E. Goncalves, and P. Parnaudeau, "High performance computing of stiff bubble collapse on CPU-GPU heterogeneous platform," Computers and Mathematics with Applications **99**, 246–256 (2021).

[50]E. Goncalves, Y. Hoarau, and D. Zeidan, "Simulation of shock-induced bubble collapse using a four-equation model," Shock Waves **29**, 221–344 (2019).

[51]J. Keller and M. Miksis, "Bubble oscillations of a large amplitude," J. Acous. Soc. Am. **68**, 628–633 (1980).

[52]J.-P. Franc and J.-M. Michel, "Fundamentals of cavitation," Kluwer Academic Publisher (2006).

[53]Y. Paquette, M. Fivel, G. Ghigliotti, E. Johnsen, and J.-P. Franc, "Fluid-structure interaction in cavitation erosion," in *10th International Symposium on Cavitation CAV2018, Baltimore, USA* (2018).

[54]E. Brujan, T. Ikeda, and Y. Matsumoto, "On the pressure of cavitation bubbles," Experimental Thermal and Fluid Science **32**, 1188–1191 (2008).

[55]E. Goncalves and D. Zeidan, "Simulation of shock-bubble interaction using a four-equation homogeneous model," in *In: Sasoh A., Aoki T., Katayama M. (eds), 31st Int. Symposium on Shock Waves. ISSW 2017. Springer, Cham.* (2019) pp. 451–458.